Received Date : 19-Aug-2016
Revised Date : 04-Oct-2016
Accepted Date : 09-Oct-2016
Article type : Research Letter

Structure and inhibition of *N*-acetylneuraminate lyase from methicillin-resistant *Staphylococcus aureus*

Rachel A North[a], Andrew J A Watson[b], F G Pearce[a], Andrew C Muscroft-Taylor[c], Rosmarie Friemann[d,e,f], Antony J Fairbanks[a,b], Renwick C J Dobson[a,g,*]

[a]Biomolecular Interaction Centre and School of Biological Sciences, University of Canterbury, Private Bag 4800, Christchurch 8041, New Zealand,
[b]Department of Chemistry, University of Canterbury, Christchurch 8140, New Zealand
[c]Protein Science and Engineering, Callaghan Innovation, University of Canterbury
[d]Department of Chemistry and Molecular Biology, University of Gothenburg, Gothenburg, Sweden
[e]Centre for Antibiotic Resistance Research (CARe), University of Gothenburg, Gothenburg, Sweden
[f]Department of Structural Biology, School of Medicine, Stanford University, California, United States of America
[g]Department of Biochemistry and Molecular Biology, Bio21 Molecular Science and Biotechnology Institute, University of Melbourne, 30 Flemington Road, Parkville, Victoria 3010, Australia

*Corresponding author:
Renwick C J Dobson
School of Biological Sciences

University of Canterbury
Private Bag 4800
Christchurch 8140
New Zealand
Fax number: +64 3 364 2590
Email: renwick.dobson@canterbury.ac.nz

Keywords: antibiotic resistance; drug discovery; inhibitor; MRSA; *N*-acetylneuraminate lyase; sialic acid degradation; structure

Abbreviations: methicillin-resistant *Staphylococcus aureus*, MRSA

Abstract

N-Acetylneuraminate lyase is the first committed enzyme in the degradation of sialic acid by bacterial pathogens. In this study, we analysed the kinetic parameters of *N*-acetylneuraminate lyase from methicillin-resistant *Staphylococcus aureus* (MRSA). We determined that the enzyme has a relatively high K_M of 3.2 mM, suggesting that flux through the catabolic pathway is likely to be controlled by this enzyme. Our data indicate that sialic acid alditol, a known inhibitor of *N*-acetylneuraminate lyase enzymes, is a stronger inhibitor of MRSA *N*-acetylneuraminate lyase than of *Clostridium perfringens N*-acetylneuraminate lyase. Our analysis of the crystal structure of ligand-free and inhibitor-bound MRSA *N*-acetylneuraminate lyase suggests that subtle dynamic differences in solution and/or altered binding interactions within the active site may account for species-specific inhibition.

1. Introduction

The term sialic acid is the designation given to a large family of nine-carbon amino sugars, the most common of which is *N*-acetylneuraminic acid [1]. Sialic acids are often found at the non-reducing termini of eukaryotic cell surface glycoconjugates, where they mediate a diverse array of biological function, including cellular interactions, recognition, and adhesion [2-4]. In the human respiratory and gastrointestinal tract, sialic acid coated glycoconjugates are highly abundant [5], whilst glucose tends to be limited in supply [6]. Thus, bacterial pathogens that colonize these environments have evolved to degrade host-derived sialic acid as a nutrient source [1,4]. The genes required for the sequestration and degradation of sialic acid are known as the '*nan nag* cluster,' and are confined to pathogenic species of bacteria and mammalian commensals [1]. The *nan nag* cluster encodes the transporter responsible for importing sialic acid into the bacterial cell and five enzymes that successively degrade sialic acid into fructose-6-phosphate, a key metabolite for glycolysis (Figure 1).

Following the importation of host derived sialic acid, the first and committed enzyme involved in sialic acid degradation is *N*-acetylneuraminate lyase. This enzyme catalyzes the retro-aldol cleavage of sialic acid into *N*-acetylmannosamine and pyruvate, a reaction that is formally the reverse of the aldol reaction where sialic acid is biosynthesized. Catalysis is proposed to involve formation of an imine (Schiff base) between the terminal ε-amine of a strictly conserved lysine residue and the C2 carbon

of the α-keto acid moiety of open form sialic acid (Figure 2) [7,8].

N-Acetylneuraminate lyase is recognized as a viable antibiotic drug target [9,10]. Deletion of the *nan*A gene coding for *N*-acetylneuraminate lyase in *Escherichia coli* [11,12], *Staphylococcus aureus* [13], *Vibrio cholerae* [14] and *Vibrio vulnificus* [6] renders the organisms incapable of growing on sialic acid *in vitro*. Moreover, *nan*A deletion strains of *V. cholerae* and *V. vulnificus* were defective for intestinal colonization in mouse models, indicative of an impaired ability to colonize and survive within the mouse intestine [1,6].

Here we present a kinetic and structural analysis of *N*-acetylneuraminate lyase from methicillin-resistant *S. aureus* (MRSA) in a new crystalline form and examine the binding of the 2*R*-diastereoisomer of sialic acid alditol. This enzyme is identical in sequence to that of a reference strain (PDB entry 4ahp) [15]. The data presented is important for further optimization of inhibitor design and synthesis, which may lead to the development of novel antibiotic drugs that target this clinically important human bacterial pathogen [16-20].

2. Materials and Methods

2.1 Cloning, expression and purification

The cloning, expression, and purification of MRSA *N*-acetylneuraminate lyase has been described previously [21].

2.2 Kinetic analysis

Kinetic analysis of MRSA *N*-acetylneuraminate lyase was performed using a lactate dehydrogenase coupled assay [22]. Using a Cary 100 Bio UV/Vis spectrophotometer (Agilent Technologies), assays were performed in duplicate.

Kinetic analysis was performed with sialic acid concentrations of 0.16 mM to 40 mM at 30 °C. Initial rate data were analyzed using OriginPro (version 8.5.1) with fitting to the Michaelis-Menten model to determine the K_M, V_{max} and the k_{cat}.

Sialic acid alditol was synthesized as a diastereomeric mixture of the 2*R*- and 2*S*-diastereoisomers, as previously described [23]. The K_i for the mixture of sialic acid alditols against MRSA *N*-acetylneuraminate lyase was determined with 0.16 mM to 20 mM of sialic acid and 0 mM to 5 mM of the alditols. These assays were performed at a physiologically relevant temperature of 37 °C. Initial rate data were analyzed using OriginPro and data were fitted to various inhibition models.

2.3 Analytical ultracentrifugation

Sedimentation velocity experiments were performed in an XL-I analytical ultracentrifuge (Beckman Coulter), using protein concentrations of 5 μM, 10 μM, and 15 μM in 20 mM Tris-HCl, pH 8.0, 100 mM NaCl. Data were collected at 280 nm, 50,000 rpm and at 20 °C. Solvent density, solvent viscosity and estimates of the partial specific volume for proteins were computed using *SEDNTERP* [24]. Data were fitted to a continuous size distribution [*c*(*s*)] model and a continuous mass distribution [*c*(*M*)] model using *SEDFIT* [25].

2.4 Crystallization

Crystallization of MRSA *N*-acetylneuraminate lyase in a ligand free form has been described previously [21]. Briefly, X-ray diffraction data was collected from a crystal grown in 25% (w/v) polyethylene glycol 3350, 200 mM ammonium sulfate, 100 mM Bis Tris, pH 5.5. Co-crystallization of MRSA *N*-acetylneuraminate lyase was performed by optimizing conditions used to grow crystals of *S. aureus N*-acetylneuraminate lyase previously [15]. The condition comprised 25% (w/v) polyethylene glycol 3350, 200 mM sodium chloride and 100 mM Tris-HCl, pH 5.5, with the addition of 5 mM of the sialic acid alditols.

2.5 Data collection, data processing and structure refinement

For X-ray data collection, crystals were mounted onto loops, soaked in cryo protectant solution containing reservoir solution made up to 20% (v/v) PEG 300 and flash cooled in liquid nitrogen. Diffraction data were collected on the MX2 beam line at the Australian Synchrotron. Indexing and integration of the data were performed using the program *iMOSFLM* [26]. Scaling and data reduction were then performed using *SCALA* [27] from the CCP4 program suite [28]. Resulting intensity data were analyzed using *PHENIX.XTRIAGE* from the Phenix program suite [29]. An estimate of the number of molecules in the asymmetric unit was obtained using the *MATTHEWS COEFFICIENT* program [30,31]. Molecular replacement was performed using *PHASER* [32]. Structure refinement was performed using *REFMAC* [33] and *PHENIX.REFINE* [29]. Iterative improvement of the map and the model was performed using alternate cycles of refinement and residue-by-residue analysis in *COOT* [34]. Water and ligand molecules were added *via COOT* and modeled into the electron density manually. Coordinate and restraint files for ligands not in the *COOT* library were generated *via SKETCHER*. PDB validation files are provided as

supplementary data.

2.6 Sequence analysis of bacterial N*-acetylneuraminate lyase enzymes*

Multiple protein sequence alignment was performed between *N*-acetylneuraminate lyase from *S. aureus*, *Gamella haemolysans*, *Haemophilus influenzae*, *Pasteurella multocida*, *Clostridium botulinum*, *E. coli*, and *C. perfringens*. This alignment was generated using *ClustalW* [35].

2.7 Small angle X-ray scattering

Small angle X-ray scattering (SAXS) data were collected on the SAXS/WAXS beam line, equipped with a Pilatus 1M detector (170 mm × 170 mm, effective pixel size, 172 × 172 μm) at the Australian Synchrotron [36]. The wavelength of the X-rays was 1.0332 Å. A sample detector distance of 1600 mm was used, providing a q range of 0.006-0.4 $Å^{-1}$. Approximately 50 μL of 10 mg/mL MRSA *N*-acetylneuraminate lyase was subjected to size exclusion chromatography on a Superdex 200 5/150 GL column, pre-equilibrated with 20 mM Tris-HCl, pH 8.0. Data were collected using a 1.5 mm glass capillary, at 20 °C, and at 2 second intervals.

Two dimensional intensity plots were radially averaged, normalized to sample transmission, and background subtracted using the Scatterbrain software (Australian Synchrotron). All subsequent SAXS analyses were performed using the ATSAS software package (version 2.3) [37]. Guinier plots were analyzed using *PRIMUS* [38] to assess data quality. Indirect Fourier transformation of the data was performed using *GNOM* [39] to generate the $P(r)$ distribution. Theoretical scattering curves of the crystal structure were generated from atomic coordinates and compared with experimental scattering curves using *CRYSOL* [40].

3. Results and Discussion

3.1 Kinetic analyses of MRSA N-*acetylneuraminate lyase reveal a high K_M for sialic acid*

Kinetic analyses of *N*-acetylneuraminate lyase enzymes demonstrate that the first step of the sialic acid degradation pathway has a low affinity for its substrate, sialic acid. The initial velocity of MRSA *N*-acetylneuraminate lyase with varying concentrations of sialic acid displays a hyperbolic dependence on substrate concentration (Figure 3 A). Appropriate controls were performed to ensure that enzyme concentration was proportional to rate and the coupling enzyme was in excess (Supplementary Figure S1). Fitting to a Michaelis-Menten kinetic model provided a K_M of 3.2 ± 0.1 mM, a V_{max} of 40.0 ± 0.2 μmol/min/mg, and a k_{cat} of 22.1 ± 0.1 s^{-1}. These values are consistent with the kinetic parameters obtained for other *N*-acetylneuraminate lyase enzymes in the literature [15,22,41-43].

Although the concentration of free sialic acid in the human respiratory and gastrointestinal tract is not well characterized, there are estimates for the concentration of sialic acid in other tissues. For example, the concentration of free sialic acid in human serum/plasma is thought to be approximately 0.0005-0.003 mM, although the total concentration (conjugated and free) is estimated to be 1.6-2.2 mM [44]. *Staphylococcus aureus* encodes a putative sodium solute symporter (gene id SAB0251), which is predicted to be responsible for the import of sialic acid into the

bacterial cell [45]. Other members of the sodium solute symporter family are known to use a sodium electrochemical gradient to drive import [46-48]. However, little is known about the *S. aureus* sodium and sialic acid symporter, including its affinity for sialic acid, the number of sodium ions co-transported, the ion specificity, or whether it uses a concentration or electrochemical gradient, or both. Given the competition for resources in the human respiratory and gastrointestinal tract and that the upper limit of available sialic acid is likely to be in the low mM range, it is unlikely that the concentration of free sialic acid being imported into the bacterial cell is higher than the K_M of *N*-acetylneuraminate lyase enzymes (2-4.1 mM).

Assuming that the concentration of free sialic acid is low compared to the K_M of *N*-acetylneuraminate lyase, this enzyme may control flux through the catabolic pathway; that is, since the concentration of sialic acid is low relative to its K_M, small changes in concentration will have a large effect on flux. This is similar to glucokinase, which has a high K_M (low binding affinity) for glucose relative to the concentration of glucose. This type of regulation by glucokinase is considered to be important for cellular homeostasis [49]. Interestingly, the closely related enzyme, dihydrodipicolinate synthase, is allosterically regulated by L-lysine, its downstream product [50]. Structurally, *N*-acetylneuraminate lyase and dihydrodipicolinate synthase enzymes are very similar, but allosteric regulation for *N*-acetylneuraminate lyase has not yet been observed.

3.2 Identification of a species-specific inhibitor of MRSA N-*acetylneuraminate lyase*

In recent years, *N*-acetylneuraminate lyase has received a considerable amount of attention from both mechanistic and structural viewpoints and has been recognized as a viable antibiotic drug target. Analogues of sialic acid have been synthesized in an effort to generate first generation inhibitors that target this enzyme. These include a mixture of the 2*R*- and 2*S*-diatereoisomers of sialic acid alditol, 4-deoxy sialic acid and 4-oxo sialic acid, which have all been shown to inhibit *N*-acetylneuraminate lyase to varying degrees. The sialic acid alditols have a hydroxyl group at the C2 position, as opposed to the ketone of sialic acid that is required for imine formation with the conserved lysine residue (Figure 3 B) [23,51,52]. Conversely, 4-deoxy sialic acid [53-55] and 4-oxo sialic acid [56] are both capable of imine formation, but because they

do not have a hydroxyl group at the C4 position, they cannot undergo retro-aldol cleavage [52]. The K_i for the sialic acid alditols is 4.1 mM [51], for 4-deoxy sialic acid it is 0.90 mM [54] and for 4-oxo sialic acid it is 0.03 mM against *C. perfringens N*-acetylneuraminate lyase [56].

Sialic acid alditol was synthesized as a diastereomeric mixture of the 2*R*- and 2*S*-diastereoisomers and its ability to inhibit MRSA *N*-acetylneuraminate lyase catalysis was tested by kinetic analysis. The K_i for the sialic acid alditols was determined to be 0.39 ± 0.01 mM (Figure 3 C) from initial velocity kinetic measurements with data fitted to the competitive model of inhibition. Un-competitive, non-competitive and mixed models of inhibition were also tested but did not fit to the data as well (Supplementary Table S1). In contrast, the value of K_i obtained for the sialic acid alditols against the *C. perfringens N*-acetylneuraminate lyase was 4.1 mM [41]. Despite having identical active site residues in regards to those that are involved in catalysis and the highly conserved active site configuration seen in *N*-acetylneuraminate lyase crystal structures, the difference in binding affinity for the inhibitor may be a result of protein dynamic differences in solution and/or altered binding interactions within the active site.

3.3 The quaternary structure of MRSA N-*acetylneuraminate lyase*

Sedimentation velocity experiments were used to characterize the quaternary structure of MRSA *N*-acetylneuraminate lyase in solution. *N*-Acetylneuraminate lyase enzymes belong to the triosephosphate isomerase (TIM)-barrel or $(\beta/\alpha)_8$-barrel subfamily of proteins, which includes dihydrodipicolinate synthase, 2-keto-3-deoxygalactonate aldolase, and 4-hydroxy-2-oxoglutarate aldolase. Nearly all of these enzymes have the same tetrameric arrangement, but interestingly, the related MRSA dihydrodipicolinate synthase enzyme exists in a monomer-dimer equilibrium in solution [57]. To characterise the oligomeric stoichiometry of MRSA *N*-acetylneuraminate lyase, experiments were performed at three concentrations. Data were fitted to a *c*(*s*) model, resulting in a distinct narrow and symmetrical peak with a sedimentation coefficient of 6.7 S at all concentrations (Figure 4 A). Other small peaks are observed at approximately 4.5 S and 9.5 S that probably arise from sample contamination (approximately 5% of the total signal). Since the ratio of these peaks, in particular the primary peak at 6.7 S, does not change across different concentrations, MRSA *N*-

acetylneuraminate lyase is a single tetrameric species in solution across the concentration range tested. This data were then fitted to a *c*(*M*) model to calculate the apparent molecular mass of the species (Figure 4 B), which was determined as 123 kDa. As the theoretical monomeric mass of MRSA *N*-acetylneuraminate lyase is 33 kDa, this is consistent with a theoretical tetrameric mass of 129 kDa. The randomly distributed residuals indicate a good fit to the data (Figure 4 C) [58].

3.4 The structure of MRSA N-*acetylneuraminate lyase in a new crystal form*

To gain molecular insight into MRSA *N*-acetylneuraminate lyase, the crystal structure was solved. X-ray diffraction data were collected to 1.70 Å and processed as described previously [21]. Following refinement, the final R_{factor} and R_{free} were reduced to 14.1% and 20.3%, respectively. All residues were modeled into electron density, except for the methionine residue at position one of each chain. A highly conserved Tyr111 residue is in the 'disallowed' region of the Ramachandran plot in each chain, as previously observed for the corresponding residue in other *N*-acetylneuraminate lyase and DHDPS structures [7,22,57,59-61]. All relevant statistics are provided in Table 1.

Consistent with the solution structure, the crystal structure of MRSA *N*-acetylneuraminate lyase is a tetramer. The tetramer can be described as a dimer of dimers, with monomers *a* and *b* forming one dimer, and monomers *c* and *d* forming the second dimer (Figure 5 A). Within the monomer of MRSA *N*-acetylneuraminate lyase, consecutive β-strands are labeled *a* through to *h* and the α-helices are labeled *A* through to *K* with the three additional C-terminal α-helices denoted as *I*, *J*, and *K*, respectively (Figure 5 B). As with all $(\beta/\alpha)_8$-barrel enzymes, the active site is located in the center of the barrel at the C-terminal end of the β-strands [62].

Mutagenesis, kinetic analysis and structural analysis of *N*-acetylneuraminate lyase enzymes in complex with substrates and substrate analogues have identified key residues involved in substrate binding and catalysis [7,8,41,42,52,63]. Sequence alignment of *N*-acetylneuraminate lyase from six bacterial species indicates the residues Ser48, Ser49, Tyr111, Lys165, Thr167 Gly189, Glu191, Asp192 and Ser208 are likely to be important for the chemistry catalyzed by MRSA *N*-acetylneuraminate lyase (Figure 6). Although Ser49 is commonly found to be a threonine in other organisms, this substitution is considered conservative as these amino acids have

similar properties. The positions of these residues are highlighted in Figure 5 C.

Our 1.70 Å structure of MRSA *N*-acetylneuraminate lyase is of a higher resolution than the previously published 2.10 Å structure of *S. aureus N*-acetylneuraminate lyase (PDB entry 4ahp) [15]. PDB entry 4ahp is missing amino acid residues Ala138 to Asn146, which forms a loop between the C-terminal end of β-strand *e* and α-helix *E* in our MRSA *N*-acetylneuraminate lyase structure. The authors propose that this loop is missing because ordering is only achieved when substrate is present in the active site, allowing the formation of an imine, which repositions the catalytically important Tyr137 residue for catalysis [15]. However, the presence of this loop in our ligand free structure of MRSA *N*-acetylneuraminate lyase suggests that ordering of this loop is unlikely to be involved in substrate binding.

Alignment of PDB entry 4ahp with our structure provides a root-mean-square difference (rmsd) of 0.49 Å based on 1094 pairs of atoms, indicating that they are highly similar. Despite this similarity, the overall shape of these structures is slightly different, with PDB entry 4ahp being longer along the axis of the tight dimer interface and shorter along the axis of the weak dimer interface. It is known that crystal environments can influence protein structure as a result of local structural differences, rigid body motion of large structural units, or conformational changes in loops, which cause protein crystals to pack differently [64-66]. It is reasonable to assume that both the unresolved loop formed by residues Ala138 to Asn146 in PDB entry 4ahp and the difference in overall shape between the structures is an artifact of crystal packing in different crystallization environments.

3.5 The solution structure of MRSA N-*acetylneuraminate lyase*

SAXS data were collected to provide information about the shape of MRSA *N*-acetylneuraminate lyase in solution. The structural parameters are summarized in Table 2. The experimental scattering data were compared with theoretical scattering curves generated from the atomic coordinates of the crystal structures of MRSA *N*-acetylneuraminate lyase and *S. aureus N*-acetylneuraminate lyase (Figure 7 A). Our MRSA *N*-acetylneuraminate lyase structure gives a better fit to the experimental scattering data than the *S. aureus N*-acetylneuraminate lyase structure [15]. It is likely that the variable shapes of these structures and the missing loop in the *S. aureus N*-acetylneuraminate lyase structure attributes to these differences. Although our crystal

structure is a more accurate representation of the structure in solution, small differences are still apparent. These slight differences may be caused by protein dynamics in solution that are constrained in the crystal [67]. That the sialic acid alditols bind to *N*-acetylneuraminate lyase enzymes from different species with altered affinities, despite highly conserved active sites, raises the possibility that protein dynamics may play a role. The $P(r)$ distribution shows a single symmetrical peak (Figure 7 B). Consistent with the crystal structure, this indicates that MRSA *N*-acetylneuraminate lyase is globular in solution.

3.6 The structure of MRSA N-*acetylneuraminate lyase in complex with a strong inhibitor*

Given the variable binding affinity of the sialic acid alditols between *N*-acetylneuraminate lyase enzymes, the structure of MRSA *N*-acetylneuraminate lyase in complex with this inhibitor was sought. Probing how inhibition occurs in MRSA *N*-acetylneuraminate lyase will aid in our understanding of why this inhibitor binds more tightly to MRSA *N*-acetylneuraminate lyase than *C. perfringens N*-acetylneuraminate lyase. The ligand free structure of MRSA *N*-acetylneuraminate lyase was crystallized in a condition that contained 200 mM ammonium sulfate. Crystallographic analysis of *N*-acetylneuraminate lyase enzymes in complex with substrates and/or substrate analogues is recognized to be difficult under such conditions [7,52]. Consistent with this, soaking and co-crystallization experiments in the presence of ammonium sulfate were unsuccessful because of a sulfate ion residing in the active site. Thus, co-crystallization was performed in previously published conditions that do not contain sulfate [15]. X-ray diffraction data was collected to 2.33 Å, processed in the space group $P2_12_12_1$ and solved by molecular replacement using the monomer of *S. aureus N*-acetylneuraminate lyase as the search model (PDB entry 4ahp) [15]. Following iterative rounds of refinement, the R_{factor} and R_{free} were reduced to 19.3% and 26.1%, respectively. This model does not include methionine at position one, or loop residues Ala138 to Asn146 in each monomer. This loop could not be modeled into the previously published ligand free structure of *S. aureus N*-acetylneuraminate lyase [15]. To ensure the absence of the loop was not a result of model bias, the structure was also solved by molecular replacement with the ligand free structure of MRSA *N*-acetylneuraminate lyase as the molecular replacement model, where this loop is resolved. Following refinement and attempts to build in

these missing residues, no electron density appeared. This further suggests that the unresolved loop in PDB entry 4ahp is likely to be an artifact of crystal packing in different environments and not a feature of substrate binding. Again, Tyr111 is in the 'disallowed' region of the Ramachandran plot. All relevant statistics are provided in Table 1.

Although sialic acid alditol was synthesized and kinetically tested as a mixture, only the 2*R*-diastereoisomer was successfully modeled and refined into the electron density within each monomer (Figure 8 A). The 2*R*-diastereoisomer of sialic acid alditol binds in the active site of MRSA *N*-acetylneuraminate lyase, which is located in the center of the $(\beta/\alpha)_8$-barrel, in a tight pocket located on the C-terminal end (Figure 8 B). The inhibitor was refined into each monomer in a relatively similar conformation (Figure 8 C), suggesting that there is little flexibility in its binding orientation.

Analysis of the binding site for the 2*R*-diastereoisomer of sialic acid alditol in MRSA *N*-acetylneuraminate lyase provides insight into how inhibition is achieved (Figure 9 A). This molecule contains a hydroxyl group at the C2 position as opposed to a ketone, thus is incapable of imine formation with Lys165. No covalent bond is formed between the C2 position of the 2*R*-diastereoisomer of sialic acid alditol and Lys165. Hydrogen bonds between Ser48 and Ser49 with the carboxylate moiety at position C1 of the 2*R*-diastereoisomer of sialic acid alditol are formed similar to complexes of *E. coli N*-acetylneuraminate lyase and pyruvate [8]. Additional hydrogen bonding interactions between MRSA *N*-acetylneuraminate lyase and the 2*R*-diastereoisomer of sialic acid alditol include the hydroxyl group at the C4 position with Gly189 and the hydroxyl group at the C6 position with Asp191 and Ser208; the latter of which also hydrogen bonds with the hydroxyl group at position C7 and the hydroxyl groups at position C7 and C9, which interact with Glu192. Importantly, all of these residues have been implicated in substrate/product binding for *N*-acetylneuraminate lyase enzymes [41,42,52,63]. In addition, Tyr252 hydrogen bonds with the carbonyl oxygen at position C5 of the 2*R*-diastereoisomer of sialic acid alditol. The corresponding residue in *E. coli N*-acetylneuraminate lyase (Phe252) lies close in proximity to the C5 carbonyl of substrate/product, but cannot form a hydrogen bond [42]. We note that the *C. perfringens* enzyme has a tyrosine at this position (Figure 6).

The structure of *H. influenzae N*-acetylneuraminate lyase in complex with the 2*R*-

diastereoisomer of sialic acid alditol has been solved. As depicted in Figure 9 B, the 2*R*-diastereoisomer of sialic acid alditol is in a relatively similar conformation within both the MRSA and *H. influenzae* active sites. The hydroxyl groups at positions C7 and C8 have been refined in different orientations, however the active site residues implicated in binding the 2*R*-diastereoisomer of sialic acid alditol are the same for both structures. Residue Tyr251 in *H. influenzae N*-acetylneuraminate lyase lies in close proximity, but does not interact, with the carbonyl oxygen at position C5 of the 2*R*-diastereoisomer of sialic acid alditol like the corresponding residue Tyr252 in MRSA *N*-acetylneuraminate lyase, which adopts an alternate conformation.

As described, the K_i for a mixture of 2*R*- and 2*S*-diastereoisomers of sialic acid alditol with MRSA *N*-acetylneuraminate lyase is 0.39 mM, which is a magnitude better than the K_i of 4.1 mM observed for the *C. perfringens* enzyme [51]. This increase in binding affinity against MRSA *N*-acetylneuraminate lyase suggests that species-specific inhibition is possible, which in this case may be attributed to very subtle protein dynamics differences in solution and/or altered binding interactions within the active site of respective enzymes.

4. Summary

We have presented a detailed investigation into the structure and inhibition of MRSA *N*-acetylneuraminate lyase. Consistent with previous literature, MRSA *N*-acetylneuraminate lyase displays a relatively high K_M, suggesting that this enzyme may regulate flux through the catabolic pathway. Kinetic analysis of MRSA *N*-acetylneuraminate lyase with a diastereomeric mixture of sialic acid alditols demonstrated that they are a stronger inhibitor for MRSA *N*-acetylneuraminate lyase than *C. perfringens N*-acetylneuraminate lyase. We have presented a structure of MRSA *N*-acetylneuraminate lyase that is of a higher resolution than a previously published *S. aureus* structure and contains new information. Subtle differences are observed between the crystal structure and the SAXS derived solution structure that may be caused by protein dynamics. To elucidate which residues are involved in binding sialic acid alditol in MRSA *N*-acetylneuraminate lyase, the structure was solved in complex with this inhibitor. A difference in the binding of this inhibitor is observed between MRSA and *H. influenzae N*-acetylneuraminate lyase.

Acknowledgements

This work was supported by grants from the Ministry of Business, Innovation and Employment (contract UOCX1208 to RCJD), the New Zealand Royal Society Marsden Fund (contract UOC1013 to RCJD), and the US Army Research Laboratory and US Army Research Office (contract W911NF-11-1-0481 to RCJD). RF acknowledges the Swedish Research Council, the Swedish Research Council Formas and the Swedish Governmental Agency for Innovation Systems (VINNOVA). We especially thank Jackie Healy for her quintessential technical support.

Figure 1. The sialic acid degradation pathway. Following the import of sialic acid into the bacterial cell, it is successively degraded into fructose-6-phosphate by *N*-acetylneuraminate lyase, *N*-acetylmannosamine-6-phosphate, *N*-acetylmannosamine-6-phosphate 2-epimerase, *N*-acetylglucosamine-6-phosphate deacetylase and glucosamine-6-phosphate deaminase.

Figure 2. Proposed catalytic mechanism of *N*-acetylneuraminate lyase. The reversible enzymatic reaction showing the involvement of a conserved lysine residue in catalysis. The conserved lysine residue is involved in the formation of an imine with the ketone at the C2 position of sialic acid in the retro-aldol sense and pyruvate in the aldol direction.

Figure 3. Kinetic analysis of MRSA *N*-acetylneuraminate lyase. (A) Kinetic analysis of MRSA *N*-acetylneuraminate lyase with sialic acid. Data were fitted to the Michaelis-Menten equation with an R^2 value of 0.99. **(B)** The chemical structure of sialic acid and the sialic acid alditols. **(C)** Kinetic analysis of MRSA *N*-acetylneuraminate lyase with varying concentrations of sialic acid and sialic acid alditol. Data best fitted to the competitive model of inhibition.

Figure 4. Sedimentation velocity analysis of MRSA *N*-acetylneuraminate lyase by analytical ultracentrifugation. Experiments were conducted at 5 μM, 10 μM and 15 μM of freshly purified protein in 20 mM Tris-HCl, pH 8.0, 100 mM sodium chloride. Data were collected at 280 nm, 50 000 rpm and 20 °C. *SEDNTERP* was used to calculate the partial specific volume of MRSA *N*-acetylneuraminate lyase (0.7404 g/ml), solvent density (1.0029 g/ml) and viscosity (0.0102 poise) [24]. Data were fitted to a *c*(*s*) and *c*(*M*) model at a resolution of 300 and a confidence level of 0.95 using *SEDFIT* [25]. **(A)** The *c*(*s*) model plotted as a function of sedimentation coefficient. Data were fitted with an *s* value ranging between 1 and 12 S. The fit resulted in a frictional ratio (f/f_0) of 1.3394. **(B)** The *c*(*M*) model plotted as a function of molecular mass (kDa). Data were fitted with a minimum mass

of 20 kDa and a maximum mass of 180 kDa. **(C)** The residuals for the *c*(*s*) distribution fits indicate randomly distributed noise.

Figure 5. The structure of MRSA *N*-acetylneuraminate lyase. (A) The tetrameric structure of MRSA *N*-acetylneuraminate lyase. Monomers are labeled *a* through *d*. The active site of each monomer is oriented towards the central cavity of the tetramer. Using the PDBePISA server [68], the oligomeric interfaces of MRSA *N*-acetylneuraminate lyase were analyzed. The tight dimer interface has 1429 Å of buried surface area, an estimate $\Delta^{i}G$ of -14.1 kcal/mol, with 22 non-covalent bonds (average of 17 hydrogen bonds and 5 hydrophobic interactions across the two tetramers in the asymmetric unit). In contrast, the weak dimer interface has 1147 Å of buried surface are, an estimate $\Delta^{i}G$ of -11.7 kcal/mol, with 27 non-covalent bonds (average of 16 hydrogen bonds and 11 hydrophobic interactions). **(B)** The monomeric structure of MRSA *N*-acetylneuraminate lyase. The β-strands are labeled *a* through *h* and the α-helices are labeled *A* through *K*. The active site is located in the center the barrel at the *C*-terminal end of the β-strands. **(C)** A stereo view of the residues that have been implicated in substrate binding and catalysis. Tyr111 is colored red as it is from the neighboring subunit.

Figure 6. Sequence alignment of *N*-acetylneuraminate lyase enzymes from six bacterial species. Highly conserved residues are highlighted with blue boxes, while those that have been implicated in substrate binding and catalysis are highlighted with black boxes. Conserved residues are numbered at the top of the sequence according to *S. aureus*.

Figure 7. SAXS data for MRSA *N*-acetylneuraminate lyase. (A) The experimental scattering profile of MRSA *N*-acetylneuraminate lyase (presented as open circles) overlaid with theoretical scattering profile of the MRSA *N*-acetylneuraminate lyase structure in magenta ($\chi^2 = 0.8$) and the theoretical scattering profile of the *S. aureus N*-acetylneuraminate lyase structure (PDB entry 4ahp) in blue ($\chi^2 = 1.9$), calculated using *CRYSOL* [40]. The Guinier plot (inset) was determined using *GNOM* [39] and gives the scattering intensity at very low scattering angles. The plot is linear suggesting that no sample aggregation and/or interparticle interference is present. **(B)** Real space distance distribution function *P*(*r*) plot determined using *GNOM* [39].

Figure 8. Sialic acid alditol in complex with MRSA *N*-acetylneuraminate lyase. (A) A stereo view of active site omit maps with the 2*R*-diastereoisomer of sialic acid alditol (yellow) within all four monomers in the asymmetric unit. Sialic acid alditol is depicted in an open chain form. The omit map was generated by removing the ligand from all active sites followed by refinement. The $2F_o$-F_c electron density was contoured at a sigma level of 1 (blue), while the F_o-F_c was contoured at a sigma level of 3 (green) and -3 (red). **(B)** A side view (left) and top view (right) of the MRSA *N*-acetylneuraminate lyase monomer with sialic acid alditol bound in the active site. The monomer is depicted as a surface representation and sialic acid alditol binds in a tight pocket at the center of the barrel. **(C)** A stereo view of sialic acid alditol from each monomer overlaid.

Figure 9. The sialic acid alditol binding site. (A) A stereo view of the sialic acid alditol 2*R*-

diastereoisomer binding site within MRSA *N*-acetylneuraminate lyase. Hydrogen bonds between the ligand and protein are indicated by black dashes. The carbons are numbered one through to nine. **(B)** A stereo view of the residues involved in binding the sialic acid alditol 2*R*-diastereoisomer in MRSA (green) and *H. influenzae* (purple) *N*-acetylneuraminate lyase overlaid. Sialic acid alditol modeled into MRSA *N*-acetylneuraminate lyase is yellow and in *H. influenzae N*-acetylneuraminate lyase it is orange. The hydroxyl groups at carbon positions seven and eight are oriented in alternative conformations.

Table 1. X-ray data collection and refinement statistics for ligand free and sialic acid alditol bound MRSA *N*-acetylneuraminate lyase.

	Ligand free MRSA *N*-acetylneuraminate lyase	Sialic acid alditol bound MRSA *N*-acetylneuraminate lyase
data collection statistics		
wavelength (Å)	0.95369	0.95369
number of images	360	360
oscillations (°)	0.5	0.5
space group	$P2_1$	$P2_12_12_1$
unit cell parameters (Å, °)	a = 80.2, b = 108.6, c = 130.8 β = 90.1	a = 81.5, b = 109.4, c = 130.8 $\alpha = \beta = \gamma = 90$
resolution range (Å)	32.3-1.70 (1.79-1.70)	46.22-2.33 (2.41-2.33)
observed reflections	823,916 (91,713)	367,079 (29,172)
unique reflections	242,175 (33,054)	49,980 (4,071)
mean $I/\sigma(I)$	8.0 (2.6)	14.2 (2.6)
completeness (%)	98.5 (92.4)	99.1 (89.8)
R_{merge}†	0.101 (0.376)	0.108 (0.812)
$R_{r.i.m.}$‡	0.118 (0.457)	0.125 (0.944)
$R_{p.i.m.}$§	0.061 (0.254)	0.063 (0.478)
wilson B value (Å^2)	15.5	27.7

molecules per asymmetric	8	4
unit	2.16	2.21
V_M (Å^3 Da^{-1})	43	44
solvent content (%)		
structure and refinement statistics		
R_{factor} (%)	14.2	19.3
R_{free} (%)	20.3	26.1
number of atoms		
protein	18,608	9,080
water	1978	177
ligands	152	84
rmsd		
bonds (Å)	0.006	0.009
angles (°)	0.0960	1.185
average B factors (Å^2)		
protein	14.5	36.5
water	19.9	33.0
ligands	21.5	37.7
Ramachandran plot, residues (%)		
favored region	96.9	96.3
allowed region	2.8	3.4
disallowed region	0.3	0.3
PDB entry	5kze	5kzd

R_{merge} † = $\sum_{hkl} \sum_i |I_i\ (hkl) - \langle I(hkl)\rangle| / \sum_{hkl}\sum_i I_i\ (hkl)$.

$R_{r.i.m}$ ‡ = $\sum_{hkl} \{N(hkl)/[N(hkl) - 1]\}^{1/2} \sum_i |I_i\ (hkl) - \langle I(hkl)\rangle| / \sum_{hkl}\sum_i I_i\ (hkl)$.

$R_{p.i.m.}$ § = $\sum_{hkl} [1/(N-1)]^{1/2} \sum_i |I_i\ (hkl) - \langle I(hkl)\rangle| / \sum_{hkl}\sum_i I_i\ (hkl)$.

Table 2. Small angle X-ray scattering structural parameters.

Parameters	MRSA *N*-acetylneuraminate lyase
q range (Å^{-1})	0.01-0.55
I(0) (cm^{-1}) [from Guinier]	0.11
I(0) (cm^{-1}) [from *P*(r)]	0.11
R_g (Å) [from Guinier]	32.8
R_g (Å) [from *P*(r)]	32.8
D_{max} (Å)	88.7

Porod volume estimate ($Å^3$)	111 611

References

[1] Almagro-Moreno, S. and Boyd, E.F. (2009). Insights into the evolution of sialic acid catabolism among bacteria. BioMed Central Evolutionary Biology 9, 118-133.

[2] Varki, A. (1993). Biological roles of oligosaccharides: all of the theories are correct. Glycobiology 3, 97-130.

[3] Schauer, R. (2000). Achievements and challenges of sialic acid research. Glycoconjugate Journal 17, 485-99.

[4] Vimr, E.R., Kalivoda, K.A., Deszo, E.L. and Steenbergen, S.M. (2004). Diversity of microbial sialic acid metabolism. Microbiology and Molecular Biology Reviews 68, 132-153.

[5] Vimr, E.R. (2013). Unified theory of bacterial sialometabolism: how and why bacteria metabolise host sialic acids. International Scholarly Research Notices Microbiology 2013, 816713.

[6] Jeong, H.G., Oh, M.H., Kim, B.S., Lee, M.Y., Han, H.J. and Choi, S.H. (2009). The capability of catabolic utilization of *N*-acetylneuraminic acid, a sialic acid, is essential for *Vibrio vulnificus* pathogenesis. Infection and Immunity 77, 3209-17.

[7] Izard, T., Lawrence, M.C., Malby, R.L., Lilley, G.G. and Colman, P.M. (1994). The three-dimensional structure of *N*-acetylneuraminate lyase from *Escherichia coli*. Structure 2, 361-369.

[8] Lawrence, M., Barbosa, J., Smith, B., Hall, N., Pilling, P., Ooi, H. and Marcuccio, S. (1997). Structure and mechanism of a sub-family of enzymes related to *N*-acetylneuraminate lyase. Journal of Molecular Biology 266, 381-399.

[9] Severi, E., Hood, D.W. and Thomas, G.H. (2007). Sialic acid utilization by bacterial pathogens. Microbiology 153, 2817-2822.

[10] von Itzstein, M. (2007). The war against influenza: discovery and development of sialidase inhibitors. Nature Reviews Drug Discovery 6, 967-974.

[11] Vimr, E.R. and Troy, F.A. (1985). Identification of an inducible catabolic system for sialic acids (*nan*) in *Escherichia coli*. Journal of Bacteriology 164, 845-53.

[12] Vogel-Scheel, J., Alpert, C., Engst, W., Loh, G. and Blaut, M. (2010). Requirement of purine and pyrimidine synthesis for colonization of the mouse intestine by *Escherichia coli*. Applied and Environmental Microbiology 76, 5181-7.

[13] Olson, M.E., King, J.M., Yahr, T.L. and Horswill, A.R. (2013). Sialic acid catabolism in *Staphylococcus aureus*. Journal of Bacteriology 195, 1779-88.

[14] Almagro-Moreno, S. and Boyd, E.F. (2009). Sialic acid catabolism confers a competitive advantage to pathogenic *Vibrio cholerae* in the mouse intestine. Infection and Immunity 77, 3807-3816.

[15] Timms, N., Windle, C.L., Polyakova, A., Ault, J.R., Trinh, C.H., Pearson, A.R., Nelson, A. and Berry, A. (2013). Structural insights into the recovery of aldolase activity in *N*-acetylneuraminic acid lyase by replacement of the catalytically active lysine with gamma-thialysine by using a chemical mutagenesis strategy. ChemBioChem: A European Journal of Chemical Biology 14, 474-81.

[16] Boyce, J.M. et al. (2005). Meticillin-resistant *Staphylococcus aureus*. Lancet Infectious Diseases 5, 653-663.

[17] McDonald, M., Hurse, A. and Sim, K.N. (1981). Methicillin-resistant *Staphylococcus aureus* bacteraemia. Medical Journal of Australia 2, 191-4.

[18] Panlilio, A.L., Culver, D.H., Gaynes, R.P., Banerjee, S., Henderson, T.S., Tolson, J.S. and Martone, W.J. (1992). Methicillin-resistant *Staphylococcus aureus* in U.S. hospitals, 1975-1991. Infection Control and Hospital Epidemiology 13, 582-6.

[19] Grundmann, H., Aires-de-Sousa, M., Boyce, J. and Tiemersma, E. (2006). Emergence and resurgence of meticillin-resistant *Staphylococcus aureus* as a public-health threat. Lancet 368, 874-85.

[20] Chambers, H.F. and Deleo, F.R. (2009). Waves of resistance: *Staphylococcus aureus* in the antibiotic era. Nature Reviews Microbiology 7, 629-41.

[21] North, R.A. et al. (2013). Cloning, expression, purification, crystallization and preliminary X-ray diffraction studies of *N*-acetylneuraminate lyase from methicillin-resistant *Staphylococcus aureus*. Acta crystallographica Section F, Structural Biology and Crystallization Communications 69, 306-12.

[22] Devenish, S.R.A. and Gerrard, J.A. (2009). The quaternary structure of *Escherichia coli N*-acetylneuraminate lyase is essential for functional

expression. Biochemical and Biophysical Research Communications 388, 107-111.

[23] Ooi, H.C., Marcuccio, S.M. and Jackson, W.R. (2000). A new preparation of the diastereoisomeric *N*-acetylneuraminic alditols. Australian Journal of Chemistry 53, 171-174.

[24] Laue, T.M., Shah, B.D., Ridgeway, T.M. and Pelletier, S.L. (1992) Analytical Ultracentrifugation in Biochemistry and Polymer Science, The Royal Society of Chemistry. Cambridge.

[25] Schuck, P. (2000). Size-distribution analysis of macromolecules by sedimentation velocity ultracentrifugation and lamm equation modeling. Biophysical Journal 78, 1606-19.

[26] Battye, T.G., Kontogiannis, L., Johnson, O., Powell, H.R. and Leslie, A.G. (2011). iMOSFLM: a new graphical interface for diffraction-image processing with MOSFLM. Acta Crystallographica Section D, Biological Crystallography 67, 271-81.

[27] Evans, P. (2006). Scaling and assessment of data quality. Acta Crystallographica Section D, Biological Crystallography 62, 72-82.

[28] Winn, M.D. et al. (2011). Overview of the CCP4 suite and current developments. Acta Crystallographica Section D, Biological Crystallography 67, 235-42.

[29] Adams, P.D. et al. (2010). PHENIX: a comprehensive Python-based system for macromolecular structure solution. Acta Crystallographica Section D, Biological Crystallography 66, 213-21.

[30] Matthews, B.W. (1968). Solvent content of protein crystals. Journal of Molecular Biology 33, 491-7.

[31] Kantardjieff, K.A. and Rupp, B. (2003). Matthews coefficient probabilities: improved estimates for unit cell contents of proteins, DNA, and protein-nucleic acid complex crystals. Protein Science 12, 1865-71.

[32] McCoy, A.J., Grosse-Kunstleve, R.W., Adams, P.D., Winn, M.D., Storoni, L.C. and Read, R.J. (2007). Phaser crystallographic software. Journal of Applied Crystallography 40, 658-674.

[33] Murshudov, G.N. et al. (2011). REFMAC5 for the refinement of macromolecular crystal structures. Acta Crystallographica Section D, Biological Crystallography 67, 355-67.

[34] Emsley, P. and Cowtan, K. (2004). Coot: model building tools for molecular graphics. Acta Crystallographica Section D, Biological Crystallography 60, 2126-32.

[35] Larkin, M.A. et al. (2007). Clustal W and Clustal X version 2.0. Bioinformatics 23, 2947-2948.

[36] Kirby, N.M., Mudie, S.T., Hawley, A.M., Cookson, D.J., Mertens, H.D.T., Cowieson, N. and Samardzic-Boban, V. (2013). A low-background-intensity focusing small-angle X-ray scattering undulator beamline. Journal of Applied Crystallography 46, 1670-1680.

[37] Konarev, P.V., Petoukhov, M.V., Volkov, V.V. and Svergun, D.I. (2006). ATSAS 2.1, a program package for small-angle scattering data analysis. Journal of Applied Crystallography 39, 277-286.

[38] Konarev, P.V., Volkov, V.V., Sokolova, A.V., Koch, M.H.J. and Svergun, D.I. (2003). PRIMUS: a Windows PC-based system for small-angle scattering data analysis. Journal of Applied Crystallography 36, 1277-1282.

[39] Svergun, D.I. (1992). Determination of the regularization parameter in indirect-transform methods using perceptual criteria. Journal of Applied Crystallography 25, 495-503.

[40] Svergun, D., Barberato, C. and Koch, M.H.J. (1995). CRYSOL - a program to evaluate X-ray solution scattering of biological macromolecules from atomic coordinates. Journal of Applied Crystallography 28, 768-773.

[41] Kruger, D., Schauer, R. and Traving, C. (2001). Characterization and mutagenesis of the recombinant *N*-acetylneuraminate lyase from *Clostridium perfringens*: insights into the reaction mechanism. European Journal of Biochemistry 268, 3831-9.

[42] Daniels, A.D. et al. (2014). Reaction mechanism of *N*-acetylneuraminic acid lyase revealed by a combination of crystallography, QM/MM simulation, and mutagenesis. American Chemical Society Chemical Biology 9, 1025-32.

[43] Stockwell, J. et al. (2016). Evaluation of fluoropyruvate as nucleophile in reactions catalyzed by *N*-acetylneuraminic acid lyase variants: scope, limitations and stereoselectivity. Organic & Biomolecular Chemistry 14, 105-12.

[44] Sillanaukee, P., Ponnio, M. and Jaaskelainen, I.P. (1999). Occurrence of sialic acids in healthy humans and different disorders. European Journal of Clinical Investigation 29, 413-425.

[45] Severi, E., Hosie, A.H.F., Hawkhead, J.A. and Thomas, G.H. (2010). Characterization of a novel sialic acid transporter of the sodium solute symporter (SSS) family and *in vivo* comparison with known bacterial sialic acid transporters. Federation of European Microbiological Societies Microbiology Letters 304, 47-54.

[46] Faham, S., Watanabe, A., Besserer, G.M., Cascio, D., Specht, A., Hirayama, B.A., Wright, E.M. and Abramson, J. (2008). The crystal structure of a sodium galactose transporter reveals mechanistic insights into Na^+/sugar symport. Science 321, 810-814.

[47] Wright, E.M., Hirayama, B.A. and Loo, D.F. (2007). Active sugar transport in health and disease. Journal of Internal Medicine 261, 32-43.

[48] Dohan, O., De la Vieja, A., Paroder, V., Riedel, C., Artani, M., Reed, M., Ginter, C.S. and Carrasco, N. (2003). The sodium/iodide Symporter (NIS): characterization, regulation, and medical significance. Endocrine Reviews 24, 48-77.

[49] Lenzen, S. (2014). A fresh view of glycolysis and glucokinase regulation: history and current status. Journal of Biological Chemistry 289, 12189-94.

[50] Blickling, S., Renner, C., Laber, B., Pohlenz, H.D., Holak, T.A. and Huber, R. (1997). Reaction mechanism of *Escherichia coli* dihydrodipicolinate synthase investigated by X-ray crystallography and NMR spectroscopy. Biochemistry 36, 24-33.

[51] Deijl, C.M. and Vliegenthart, J.F. (1983). Configuration of substrate and products of *N*-acetylneuraminate pyruvate-lyase from *Clostridium perfringens*. Biochemical and Biophysical Research Communications 111, 668-74.

[52] Barbosa, J. et al. (2000). Active site modulation in the *N*-acetylneuraminate lyase sub-family as revealed by the structure of the inhibitor-complexed *Haemophilus influenzae* enzyme. Journal of Molecular Biology 303, 405-421.

[53] Hagedorn, H.W. and Brossmer, R. (1986). Synthesis and biological properties of *N*-acetyl-4-deoxy-D-neuraminic acid. Helvetica Chimica Acta 69, 2127–2132.

[54] Zbiral, E., Kleineidam, R.G., Schreiner, E., Hartmann, M., Christian, R. and Schauer, R. (1992). Elucidation of the topological parameters of *N*-acetylneuraminic acid and some analogues involved in their interaction with the *N*-acetylneuraminate lyase from *Clostridium perfringens*. The Biochemical Journal 282, 511-6.

[55] Ooi, H.C., Marcuccio, S.M. and Jackson, W.R. (1999). An alternative synthesis of *N*-acetyl-4-deoxyneuraminic acid. Australian Journal of Chemistry 52, 937-940.

[56] Gross, H.J. and Brossmer, R. (1988). Inhibition of *N*-acetylneuraminate lyase by *N*-acetyl-4-oxo-D-neuraminic acid. Federation of European Biochemical Societies Letters 232, 145-147.

[57] Burgess, B.R. et al. (2008). Structure and evolution of a novel dimeric enzyme from a clinically important bacterial pathogen. Journal of Biological Chemistry 283, 27598-603.

[58] Lebowitz, J., Lewis, M.S. and Schuck, P. (2002). Modern analytical ultracentrifugation in protein science: a tutorial review. Protein Science 11, 2067-79.

[59] Mirwaldt, C., Korndorfer, I. and Huber, R. (1995). The crystal structure of dihydrodipicolinate synthase from *Escherichia coli* at 2.5 Å resolution. Journal of Molecular Biology 246, 227-39.

[60] Dobson, R.C., Griffin, M.D., Jameson, G.B. and Gerrard, J.A. (2005). The crystal structures of native and (S)-lysine-bound dihydrodipicolinate synthase from *Escherichia coli* with improved resolution show new features of biological significance. Acta Crystallographica Section D, Biological Crystallography 61, 1116-24.

[61] Kefala, G. et al. (2008). Crystal structure and kinetic study of dihydrodipicolinate synthase from *Mycobacterium tuberculosis*. The Biochemical Journal 411, 351-60.

[62] Wierenga, R.K. (2001). The TIM-barrel fold: a versatile framework for efficient enzymes. Federation of European Biochemical Societies Letters 492, 193-8.

[63] Huynh, N. et al. (2013). Structural basis for substrate specificity and mechanism of *N*-acetyl-D-neuraminic acid lyase from *Pasteurella multocida*. Biochemistry 52, 8570-9.

[64] Eyal, E., Gerzon, S., Potapov, V., Edelman, M. and Sobolev, V. (2005). The limit of accuracy of protein modeling: influence of crystal packing on protein structure. Journal of Molecular Biology 351, 431-42.

[65] Bertrand, J.A., Fanchon, E., Martin, L., Chantalat, L., Auger, G., Blanot, D., van Heijenoort, J. and Dideberg, O. (2000). "Open" structures of MurD: domain movements and structural similarities with folylpolyglutamate synthetase. Journal of Molecular Biology 301, 1257-66.

[66] Taylor, P., Dornan, J., Carrello, A., Minchin, R.F., Ratajczak, T. and Walkinshaw, M.D. (2001). Two structures of cyclophilin 40: folding and fidelity in the TPR domains. Structure 9, 431-8.

[67] Griffin, M.D. et al. (2008). Evolution of quaternary structure in a homotetrameric enzyme. Journal of Molecular Biology 380, 691-703.

[68] Krissinel, E. and Henrick, K. (2007). Inference of macromolecular assemblies from crystalline state. Journal of Molecular Biology 372, 774-97.

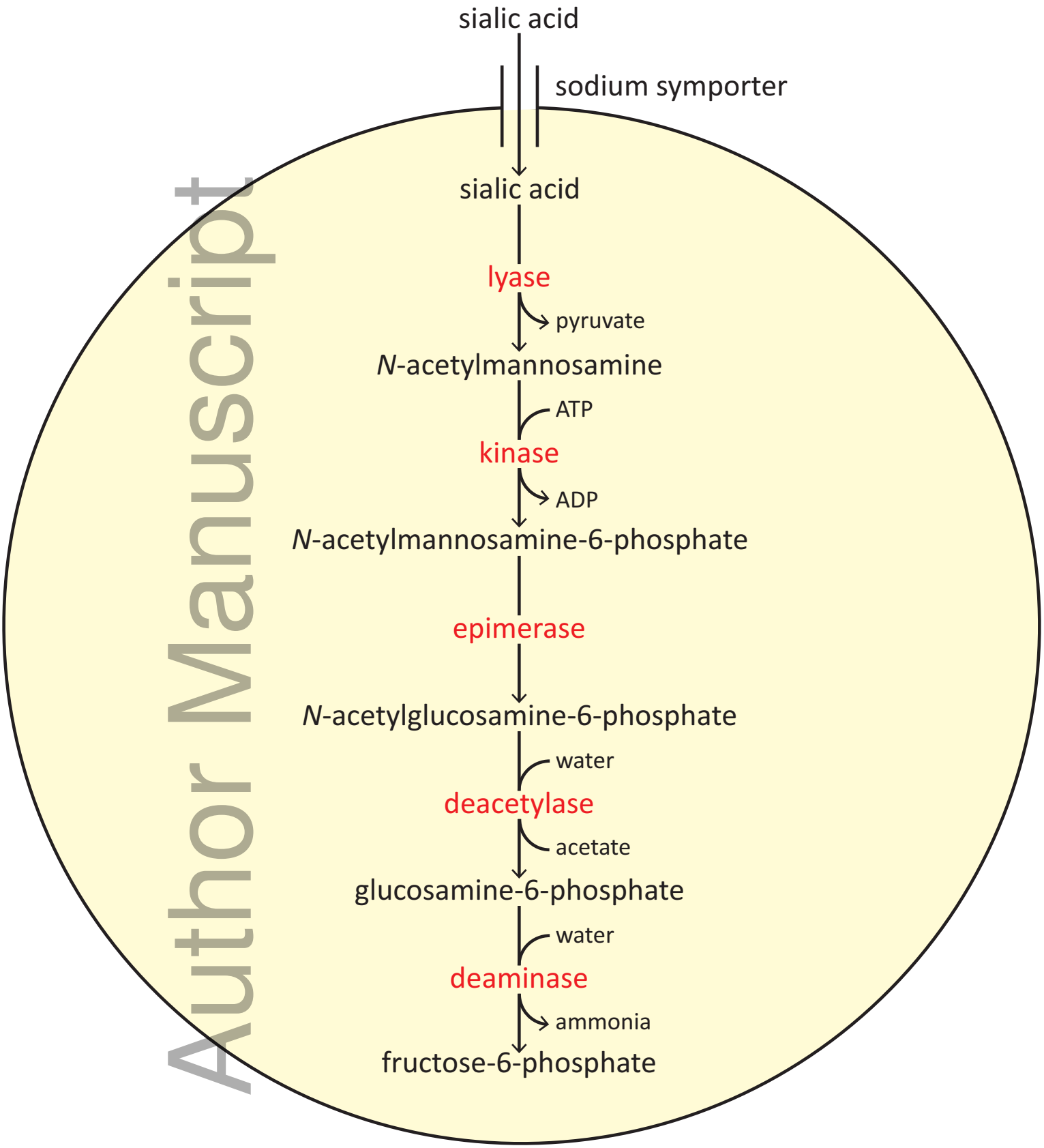

feb2_12462_f1.eps

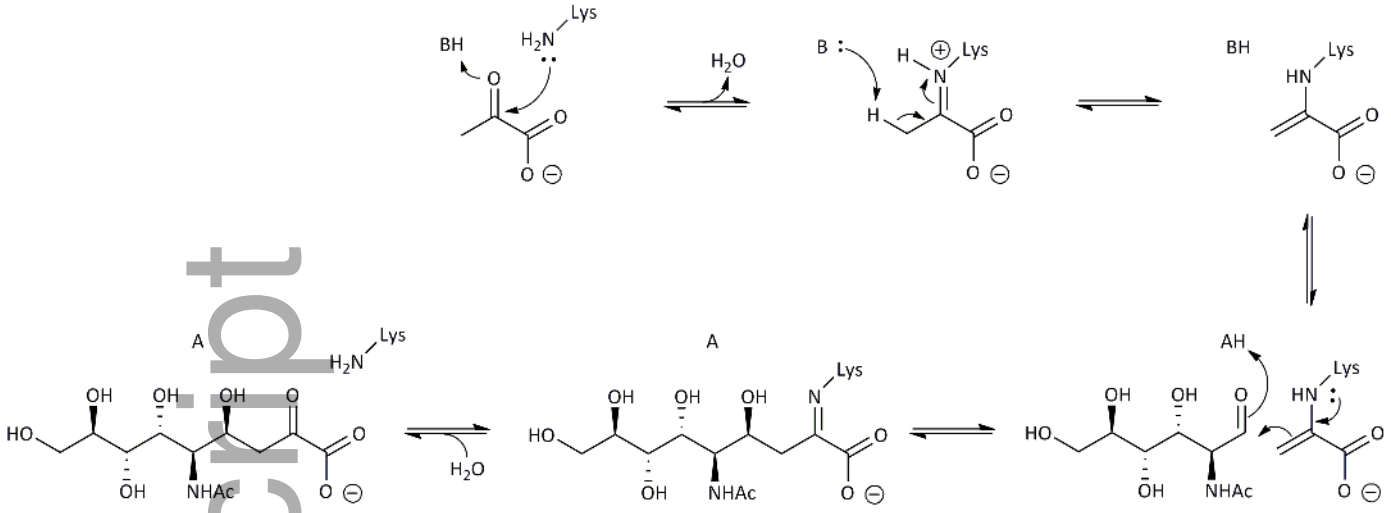

feb2_12462_f2.tif

A

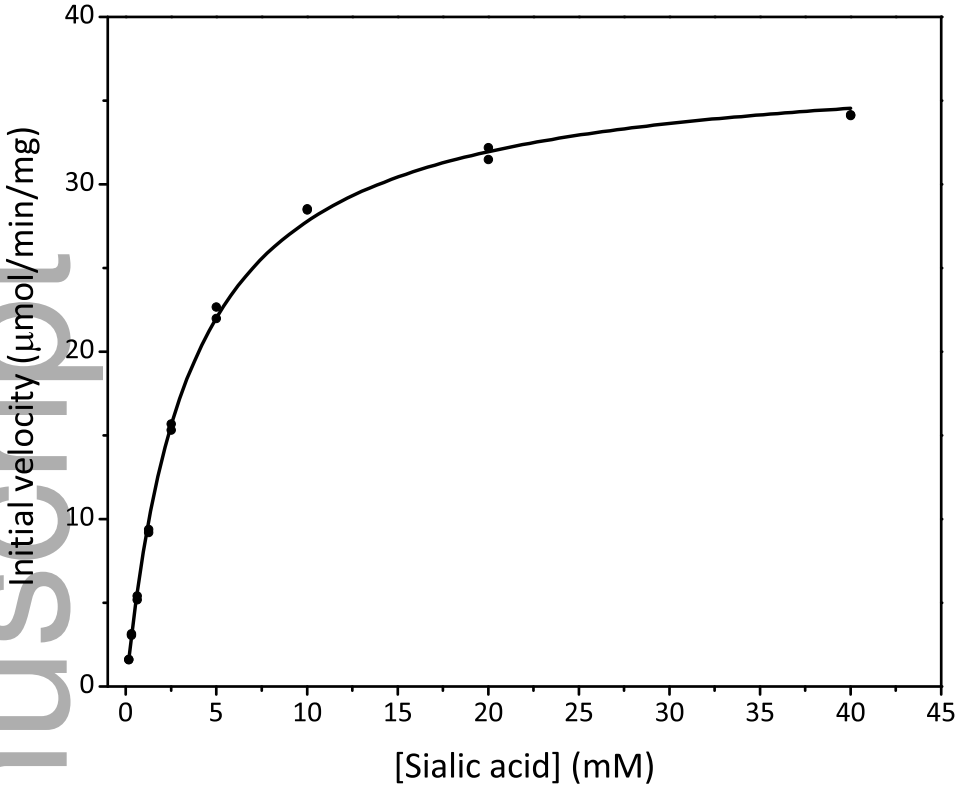

B

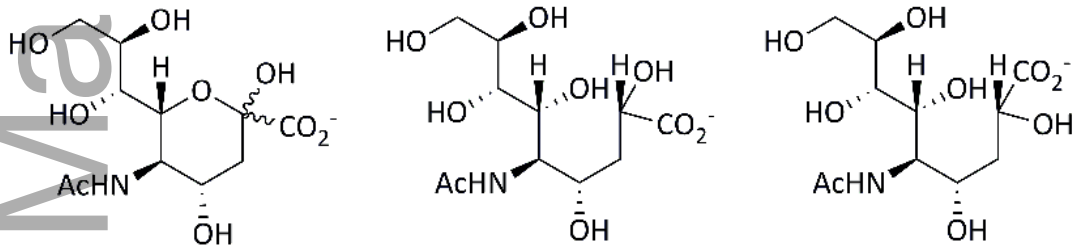

C

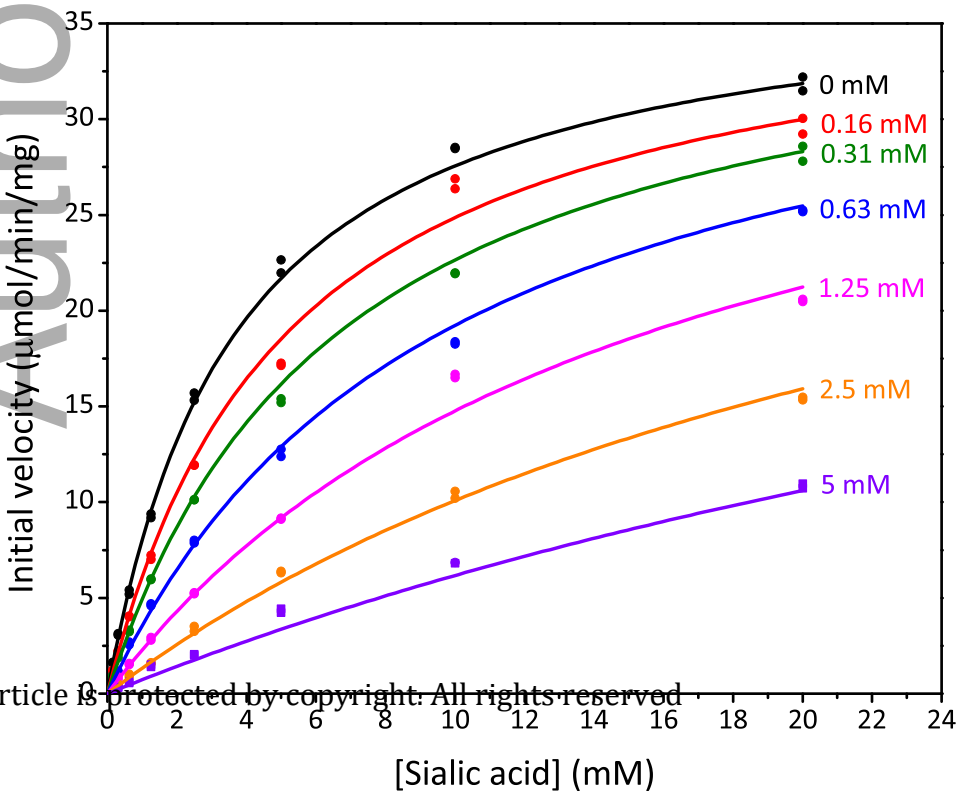

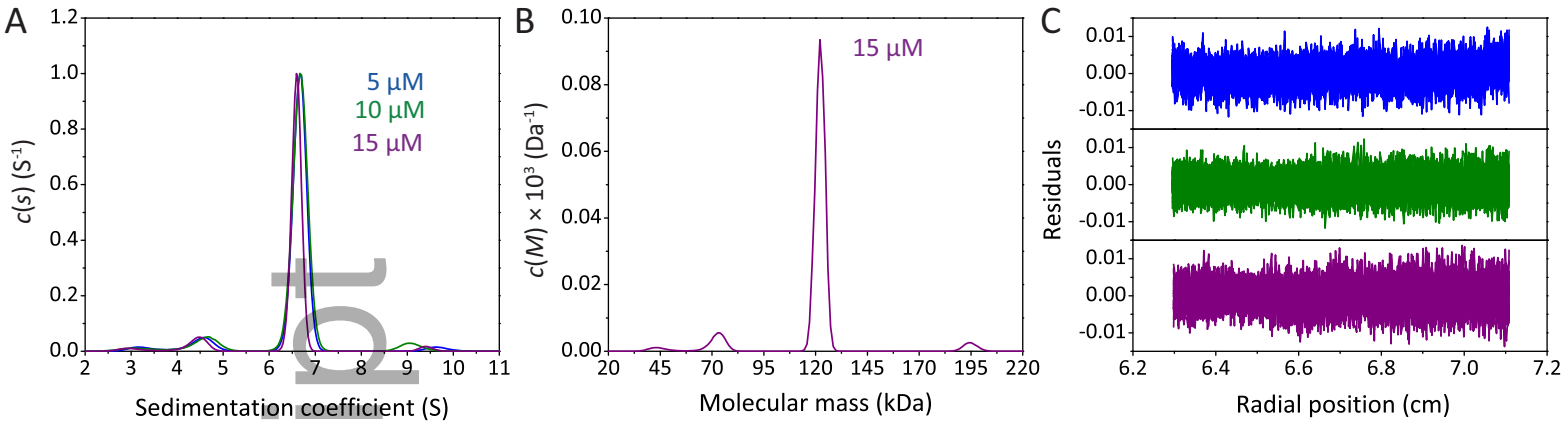

feb2_12462_f4.eps

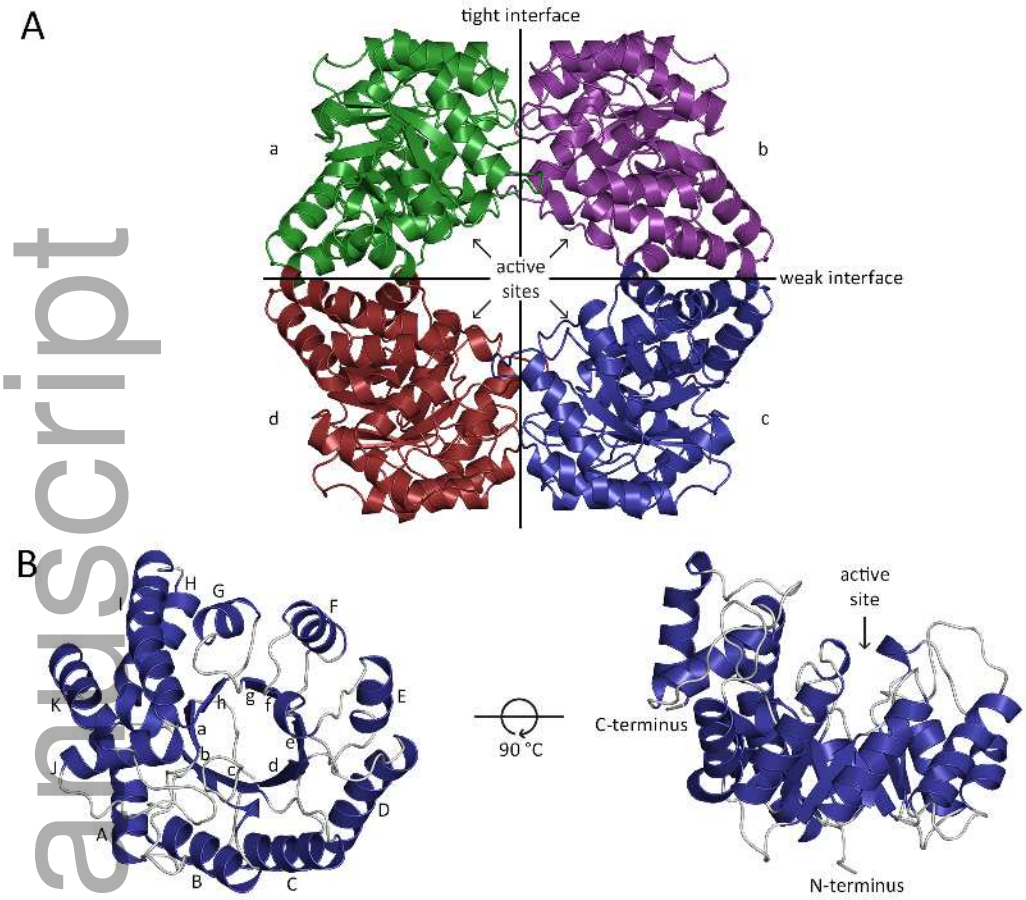

feb2_12462_f5.tif

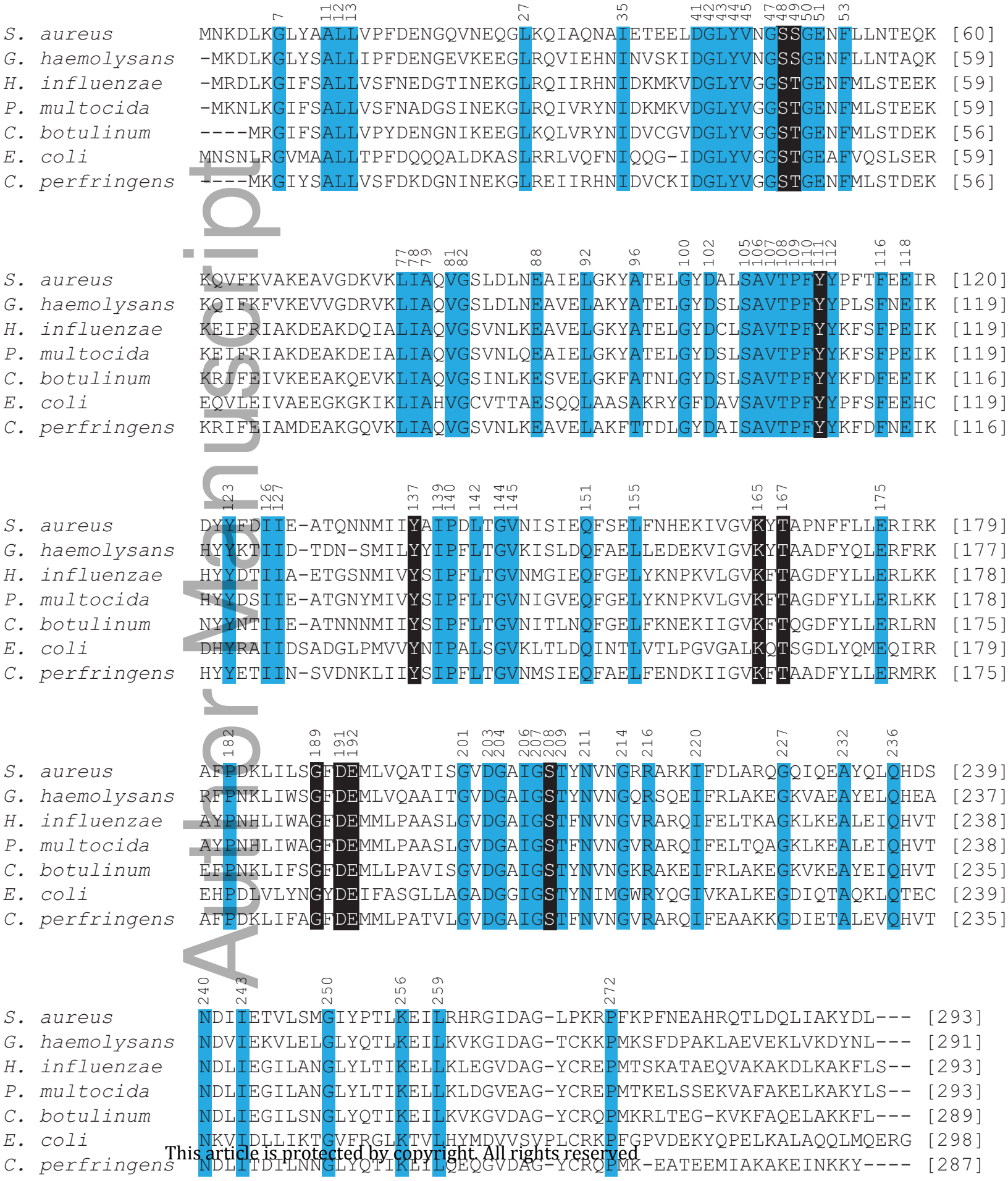

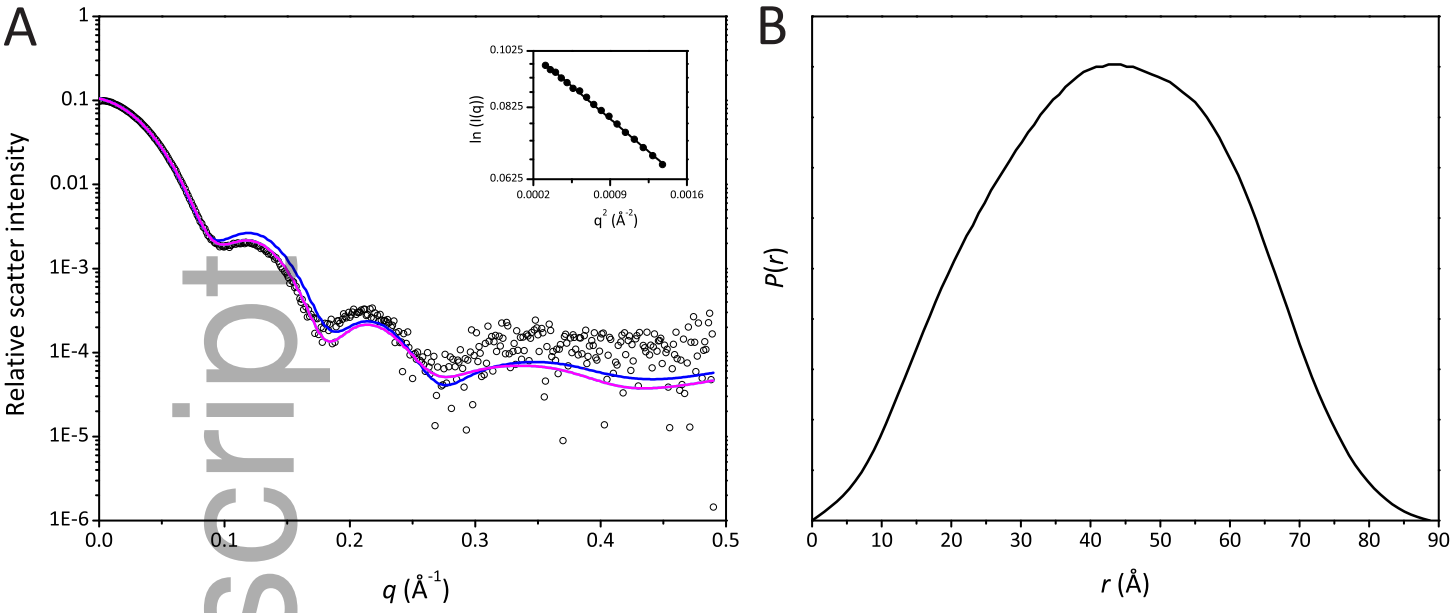

feb2_12462_f7.eps

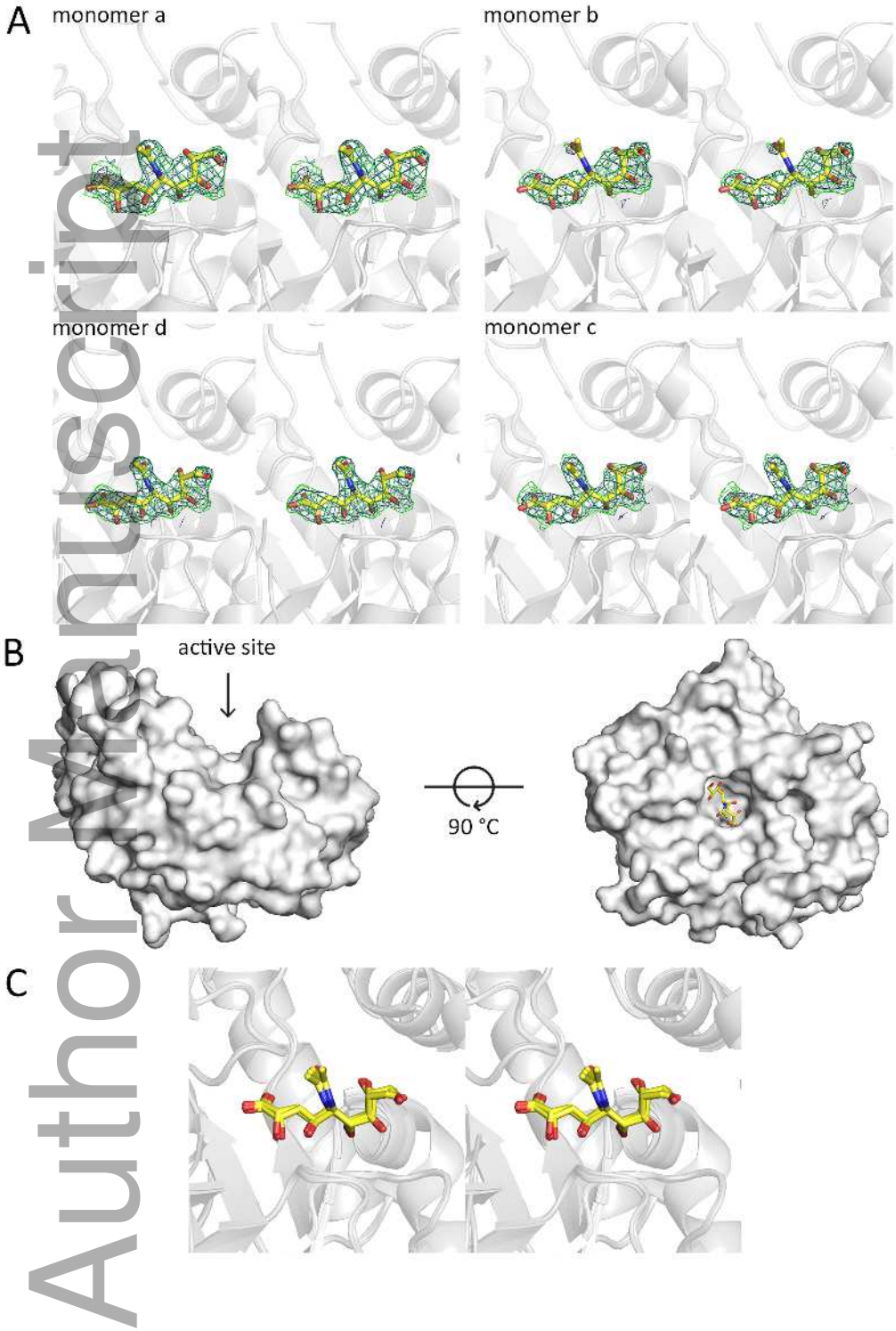

feb2_12462_f8.tif

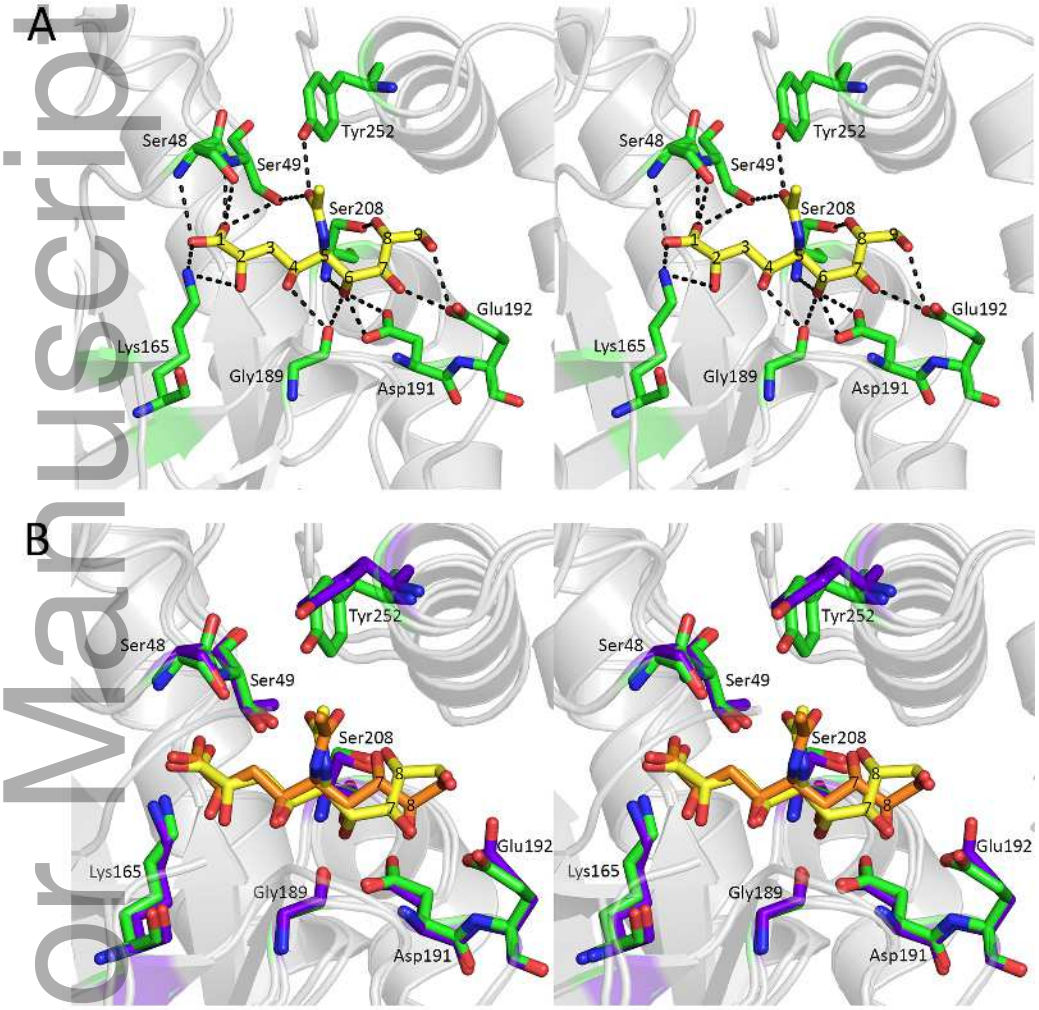

feb2_12462_f9.tif